Geophysical Journal International

Geophys. J. Int. (2018) **213,** 1360–1373
Advance Access publication 2018 February 15
GJI Geodynamics and tectonics

doi: 10.1093/gji/ggy061

Tectonic stress orientations and magnitudes, and friction of faults, deduced from earthquake focal mechanism inversions over the Korean Peninsula

Inho Soh,[1] Chandong Chang,[1] Junhyung Lee,[2] Tae-Kyung Hong[2] and Eui-Seob Park[3]

[1]*Department of Geology, Chungnam National University, Daejeon* 34134, *South Korea. E-mail: cchang@cnu.ac.kr*
[2]*Department of Earth System Sciences, Yonsei University, Seoul* 03722, *South Korea*
[3]*Center for Deep Subsurface Research, Korea Institute of Geoscience and Mineral Resources, Daejeon* 34132, *South Korea*

Accepted 2018 February 14. Received 2017 December 28; in original form 2017 August 4

SUMMARY

We characterize the present-day stress state in and around the Korean Peninsula using formal inversions of earthquake focal mechanisms. Two different methods are used to select preferred fault planes in the double-couple focal mechanism solutions: one that minimizes average misfit angle and the other choosing faults with higher instability. We invert selected sets of fault planes for estimating the principal stresses at regularly spaced grid points, using a circular-area data-binning method, where the bin radius is optimized to yield the best possible stress inversion results based on the World Stress Map quality ranking scheme. The inversions using the two methods yield well constrained and fairly comparable results, which indicate that the prevailing stress regime is strike-slip, and the maximum horizontal principal stress (S_{Hmax}) is oriented ENE–WSW throughout the study region. Although the orientation of the stresses is consistent across the peninsula, the relative stress magnitude parameter (R-value) varies significantly, from 0.22 in the northwest to 0.89 in the southeast. Based on our knowledge of the R-values and stress regime, and using a value for vertical stress (S_{v}) estimated from the overburden weight of rock, together with a value for the maximum differential stress (based on the Coulomb friction of faults optimally oriented for slip), we estimate the magnitudes of the two horizontal principal stresses. The horizontal stress magnitudes increase from west to east such that $S_{\mathrm{Hmax}}/S_{\mathrm{v}}$ ratio rises from 1.5 to 2.4, and the $S_{\mathrm{hmin}}/S_{\mathrm{v}}$ ratio from 0.6 to 0.8. The variation in the magnitudes of the tectonic stresses appears to be related to differences in the rigidity of crustal rocks. Using the complete stress tensors, including both orientations and magnitudes, we assess the possible ranges of frictional coefficients for different types of faults. We show that normal and reverse faults have lower frictional coefficients than strike-slip faults, suggesting that the former types of faults can be activated under a strike-slip stress regime. Our observations of the seismicity, with normal faulting concentrated offshore to the northwest and reverse faulting focused offshore to the east, are compatible with the results of our estimates of stress magnitudes.

Key words: Friction; Continental neotectonics; Dynamics: seismotectonics; Dynamics and mechanics of faulting; Intra-plate processes.

1 INTRODUCTION

Earthquakes are the clearest indicators of stress within the crust. Earthquake focal plane mechanisms are related to the characteristics of the prevailing stress state of actively deforming crust at seismogenic depths (Zoback 1992; Scholz 2002), and various methods have been proposed to derive the stress state from inversions of focal mechanism data (Angelier 1979; Gephart & Forsyth 1984; Michael 1984; Rivera & Cisternas 1990; Hardebeck & Michael 2006). These techniques assume that the earthquakes used in the inversion are clustered in a region subject to a uniform stress field, and act to minimize the average angle (misfit angle) between the earthquake slip vectors and the orientation of the maximum shear stress on the faults. The inversion process yields four stress tensor parameters: the orientations of the three principal stresses (S_1, S_2 and S_3) and the relative magnitude of S_2 with respect to the maximum differential stress (defined by the R-value $= (S_1 - S_2)/(S_1 - S_3)$). This type of stress inversion has been used extensively in the literature to

characterize the crustal stress state for a variety of tectonic settings (Zoback 1992; Amato & Montone 1997; Plenefisch & Bonjer 1997; Townend & Zoback 2006; Li *et al.* 2015), which demonstrated systematic heterogeneity in regional stress orientations depending on the tectonic environment.

Stress inversions can be used to determine the relative magnitudes of tectonic stresses. Additional assumptions, or independent data, are required to estimate absolute magnitudes of tectonic stresses, which are important for studies of fault mechanics; for example, determining fault friction (Scholz 2002). Previous workers have taken various approaches to this problem. For example, Zoback (1992) and Plenefisch & Bonjer (1997) assumed that the maximum magnitude of differential stress ($S_1 - S_3$) is limited by the friction on optimally oriented faults for slip under a given stress state, whereas Rivera & Kanamori (2002), and later Hsu *et al.* (2010), used an independently evaluated parameter related to the ratio of minimum to maximum principal stress (S_3/S_1). Although some ambiguity exists because of variable stress regimes, such approaches in estimating absolute stress magnitudes reveal an appreciable variation in the friction on faults.

In this study, we investigate stress heterogeneity in the Korean Peninsula and its implications for fault mechanics. We use earthquake focal mechanism inversions to estimate both the orientations and absolute magnitudes of the stresses at seismogenic depths, in order to understand the characteristics of the stress regime. A number of researchers have investigated the stress state in Korea, which is situated in an intraplate zone near the eastern edge of the Eurasian plate (Jun 1991; Park *et al.* 2007; Chang *et al.* 2010; Hong & Choi 2012), and a subset of the stress data derived from these studies was published in the 2016 release of the World Stress Map (WSM) database (Heidbach *et al.* 2016). Unfortunately, most these stress data are derived from single focal mechanism solutions and an assumption that the P- and T-axes lie along the orientations of the maximum and minimum principal stresses, respectively. A single focal mechanism solution, normally expressed in the form of a stereographic projection of the rock strain that occurs upon fault slip, only gives information on the maximum and minimum strain axes. Since the strain axes depend on the orientation of the pre-existing fault that was activated, they do not necessarily coincide with the orientations of the regional stress axes. The WSM estimates that the assumption that the orientations of the P- and T-axes are equivalent to the principal stress axes, results in uncertainties of at least $\pm 25^{\circ}$ in estimates of the orientation of regional stresses (Barth *et al.* 2016).

More reliable stress estimates can be obtained using inversions of multiple focal mechanism solutions clustered in a uniform stress field. Indeed, Park *et al.* (2007) performed inversions using 71 focal mechanisms ($1.9 \leq M \leq 5.2$) from the Korean Peninsula. Their results indicate that the maximum principal stress is oriented E–W, and that there is a predominantly strike-slip faulting regime throughout the region. Although it is normally expected that one of the principal stress axes will be vertical in a relatively stable tectonic province, Park *et al.* (2007) reported that none of the principal stress axes they obtained was vertical. This may be a result of inappropriate binning of focal mechanism solutions or an insufficient amount of data used in the inversion.

We carried out stress inversions using 152 published earthquake focal mechanism solutions. We used the WSM ranking scheme to assess the quality of our data and designate bins for the inversions. Our use of a large catalogue of earthquakes and our stringent data quality assessment increases the reliability of the inversion results. We also use our inversions, together with additional independent constraints, to estimate absolute magnitudes of stress in the Korean Peninsula and to describe the spatial variation in tectonic stress. Using the complete stress tensors obtained through the inversion process, we then attempt to relate stress heterogeneity in the Korean Peninsula to fault mechanics, in particular the friction on faults and the types of faults.

2 DATA COMPILATION AND INVERSION STRATEGY

We compiled earthquake focal mechanisms from the WSM (Heidbach *et al.* 2016) and the studies of Park *et al.* (2007), Rhie & Kim (2010), Hong & Choi (2012), Hong *et al.* (2015) and Kim *et al.* (2016b). These focal mechanism solutions were determined either from long period waveform inversion for most of $>M$ 3 earthquakes, or from *P*-wave first arrival polarity and *S*/*P* amplitude ratio analysis for the smaller magnitude earthquakes. The focal mechanism solutions derived from the waveform inversion were quite well constrained due to the characteristics of moderate-sized intraplate seismicity, which shows relatively high signal-to-noise ratio in seismic waves (Hong *et al.* 2015). The quality of focal mechanisms derived from polarity analyses depends mainly on distribution of seismic network, which governs the coverage of source-station azimuths. More than 180 seismic stations densely distributed over the Korean Peninsula and adjacent islands cover source-station azimuths sufficiently to constrain reliable focal mechanism solutions on- and offshore. For details of seismic station distribution in and around the Korean Peninsula, see Hong *et al.* (2015).

We screened the data based on the following two rules. First, we only use earthquakes with magnitudes of $M \geq 2.5$, because this is the lower bound of the WSM criterion for C-quality focal mechanisms (Barth *et al.* 2016), and events of smaller magnitudes may be less reliable representative of the stress field. Second, we only use main-shock earthquake data and exclude aftershock data, which may reflect temporal stress perturbations associated with Coulomb stress transfer (Stein 1999). In Korea, a few cases were reported, in which aftershocks occurred several hours up to several days after the main earthquakes in regions around epicentres (within ~10 km radius) (e.g. Kang & Baag 2004; Kim *et al.* 2010; Kim *et al.* 2016a). For example, an M 5.8 main shock that occurred in southeast Korea in September 2016 was followed by a swarm of more than 600 aftershocks (Kim *et al.* 2016a; Hong *et al.* 2017). We exclude all of these aftershocks, even though some had magnitudes of $M > 2.5$. Our final data catalogue includes 152 focal mechanisms for earthquakes of magnitude $2.5 \leq M \leq 5.8$ that occurred between 1976 and 2016 (Fig. 1a). The events occur throughout the seismogenic crust up to a depth of ~20 km, with an average focal depth of 11.2 ± 5.0 km (Fig. 1b).

Fig. 1 shows the distribution of earthquakes in the Korean Peninsula. Faulting styles of individual earthquakes are classified based on P-, B-, and T-axis plunges following the classification suggested by Zoback (1992), in which normal faulting event is defined when P-plunge $>52^{\circ}$ and T-plunge $<35^{\circ}$; reverse faulting event when P-plunge $<35^{\circ}$ and T-plunge $>52^{\circ}$; and strike-slip event when P-plunge $<40^{\circ}$, T-plunge $<20^{\circ}$ and B-plunge $>45^{\circ}$. Although there are several locations where the earthquake population is relatively dense, earthquakes generally occur throughout the country. Strike-slip events predominate, comprising 63 per cent of the total compiled earthquakes, followed by reverse (21 per cent) and normal (13 per cent) faulting earthquakes. Normal faulting events occur mainly offshore to the northwest, whereas reverse faulting events

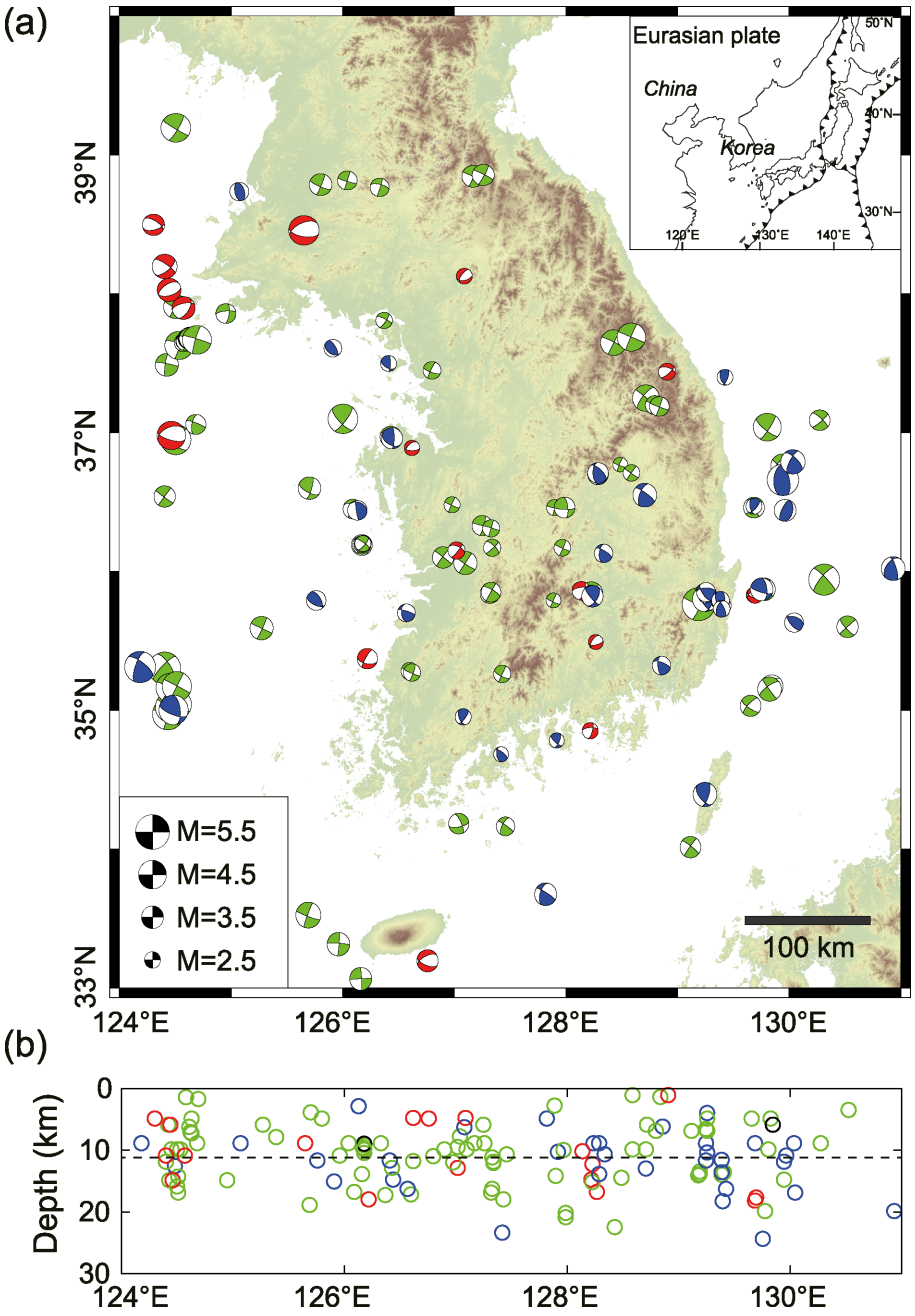

Figure 1. Map of the Korean Peninsula showing the 152 earthquake focal mechanisms used in this study. (a) Focal mechanisms are coloured according to the type of faulting: normal (red), strike-slip (green) and reverse (blue). (b) Earthquakes are projected onto an E–W profile, plotted at the focal depth. Seismicity occurs up to a depth of ∼20 km; the average focal depth is 11.2 km, as marked by a dashed line in (b). Vertical exaggeration of (b) is ∼5.

occur offshore to the east. As we will show later, this pattern will be reflected in our stress inversion results, which show spatial variation in the stress field, especially in terms of the magnitudes of the stress.

The P- and T-axes of earthquake focal mechanism represent the strain field around the slipped fault. Although they are not equivalent to the principal stress axes, we use them as a preliminary estimate of the azimuth of the maximum horizontal stress. Fig. 2 shows a histogram of P-axis azimuths (for strike-slip and reverse faulting) and B-axis azimuths (for normal faulting). It should be noted that the dispersion in the strain axes is greater than 50° and that there is a large uncertainty in estimates of the orientation of the maximum horizontal stress based on this type of data (±25° for $M \geq 2.5$ earthquakes; Barth *et al.* 2016); however, the gross pattern indicates an ENE–WSW-oriented stress. This suggests that the orientation of the stress field may be fairly consistent across Korea.

We use the stress inversion technique developed by Michael (1984, 1987), which employs a straightforward linear inversion algorithm. An important assumption of this type of inversion is that there is a uniform stress field throughout the region where the earthquakes included in the inversion are located. The inversion method provides an estimate of uncertainty in stress results using a statistical bootstrap resampling technique (Michael 1987; Delvaux & Barth 2010). For earthquake data, there is a well-known ambiguity as to which nodal plane represents the true fault plane in double-couple focal mechanisms; therefore, there are several stages to the inversion process before we obtain final results. We attempt two different

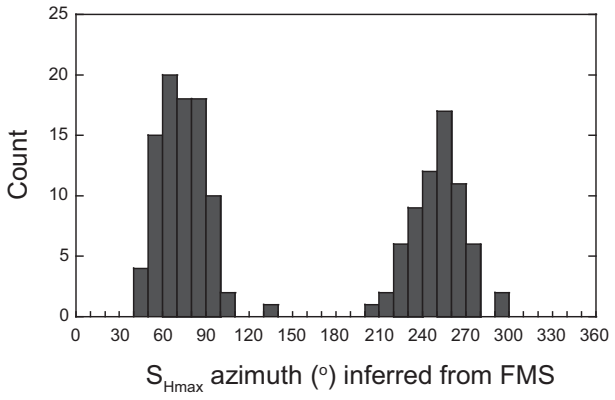

Figure 2. Histogram showing the distribution of the maximum horizontal stress (S_{Hmax}) azimuths inferred from individual focal mechanisms.

approaches to tackle the fault plane ambiguity. The primary method we use to determine preferred fault planes is to use slip vector misfit angle (called 'misfit angle method' hereafter). We use this method because the current WSM stress quality ranking scheme is partly based on the average misfit angle, which is presented in Table 1. Later, we will use a second method (called 'instability method' hereafter), in which preferred fault planes are selected based on a parameter defining instability of each nodal plane in individual focal mechanism solutions (Vavryčuk 2014), to check consistency and reliability of both stress inversion results.

For the misfit angle method, we first arbitrarily select one nodal plane for each individual focal mechanism, and run the inversion to obtain an initial estimate of the stress tensor. We then infer a slip vector from the initial stress tensor and compare it with the slip vector for each of the two nodal planes for every earthquake focal mechanism. We choose the best-fit nodal plane for each event as the preferred fault plane. Finally, we invert the focal mechanism data using our preferred fault planes to obtain the final stress tensor.

If there is spatial heterogeneity in the stress field, the way the data are binned can have a significant impact on the outcome and reliability of the inversion (Hardebeck & Michael 2004). The larger the bin, the more focal mechanism data points it can include; this generally improves the quality of the inversion results. However, if the bin is too large, and there is spatial heterogeneity in the orientation of the stress field, this may result in large misfit angles (the average angle between the earthquake slip vectors and the orientation of the maximum shear stress on the faults obtained through the inversion). The best stress field estimates come from inversions of a large amount of data (>15), which yield small ($\leq 12^\circ$) misfit angles (Barth *et al.* 2016); we summarize the WSM ranking scheme for the quality of inversion results in Table 1.

To avoid any bias in the creation of bins, we use the following method to optimize the size of the bins in order to yield the best quality stress results. We first grid our study region at 1° intervals. Each grid point marks the centre of a circular area, or bin, and we run our inversion for each grid point for all focal mechanism data lying within that area. We run repeat inversions, varying the radius of the circular bins from 30 to 150 km, in steps of 5 km. As the radius increases, the circular area would contain a larger number of focal mechanism data, improving stress data quality. However, the incorporation of a larger number of data simultaneously tends to increase average misfit angle because of potential stress heterogeneity, which tends to deteriorate stress data quality. Thus, there should be an optimum radius that yields highest quality stress data based on the WSM ranking scheme for a given set of focal mechanism data. This binning strategy ensures that we obtain reliable stress field results.

We show two examples of our binning procedure in Fig. 3. For grid point 36° N, 127° E (Fig. 3a), when the bin radius is between 40 and 75 km, ≤ 12 data points are inverted and the quality of the stress inversion is low (B-ranked according to the WSM ranking scheme) due to the insufficient number of data points. We also plot key inversion results for the best-fit stress tensor. As the radius is increased across this interval, the azimuth of S_1 varies significantly, and the plunge of S_2 deviates from vertical by $\sim 10^\circ$. When the bin radius is between 80 and 110 km, both the number of data points in each bin and the size of the resultant misfit angle meet A-quality criteria. The S_1 azimuth remains largely constant and S_2 is near vertical when the radius is <100 km. As we increase the radius further, the average misfit angle also increases ($\geq 12^\circ$) and the quality of the inversion result falls back into the B-quality range. This is because the radius is large enough that some of the focal mechanisms may lie in a different stress regime, hence the larger misfit angles. The optimum bin radius is 90 km in that this radius yields the lowest misfit angle among the A-quality inversions. In a second example, for grid point 36° N, 128° E (Fig. 3b), the quality of the inversion result varies significantly with the bin radius. For a radius of 55–60 km, too few data points are included in the bins and the stress inversion has a B-quality ranking. In this case, the plunge of S_2 deviates from vertical by 16°. A-quality criteria are met with a bin radius of 65–85 km or 100–110 km. For these bin radii the plunge of S_2 is quite consistent and lies close to the vertical (7° deviation). For this grid point, we chose an optimum 80 km bin radius, because the misfit angle is lowest for this bin size.

3 STRESS INVERSION RESULTS

Our inversion results projected in stereonets are shown in Fig. 4(a) with the 95 per cent confidence regions. The confidence regions are derived by 1000 times random bootstrap resampling of the fault planes. The best-fit stress orientations are indicated by plus symbols and also summarized in Table 2. The inversion yields A- and B-quality stress results based on the WSM quality ranking scheme for all the grid points analysed; out of a total 23 grid points, A-quality results are obtained at 7 locations and B-quality results at 16 locations. While the quality of the resultant stress field is assessed both based on the number of binned data points and the misfit angle, the limiting factor in our study is the number of data points. For A-quality stress results, the number of focal mechanism solutions inverted in individual bins ranges from 16 to 28, whereas for B-quality stress results the number of inverted focal mechanisms barely exceeds the lower bound for a B-quality ranking (≥ 8 data points) at roughly half of the grid points analysed. This

Table 1. World Stress Map ranking scheme for the reliability of stress inversion results (Barth *et al.* 2016).

Stress data quality	Number of focal mechanisms inverted	Average misfit angle	Uncertainty in S_{Hmax} azimuth
A	≥ 15	$\leq 12^\circ$	$\leq \pm 15^\circ$
B	≥ 8	$\leq 20^\circ$	$\leq \pm 15$–20°

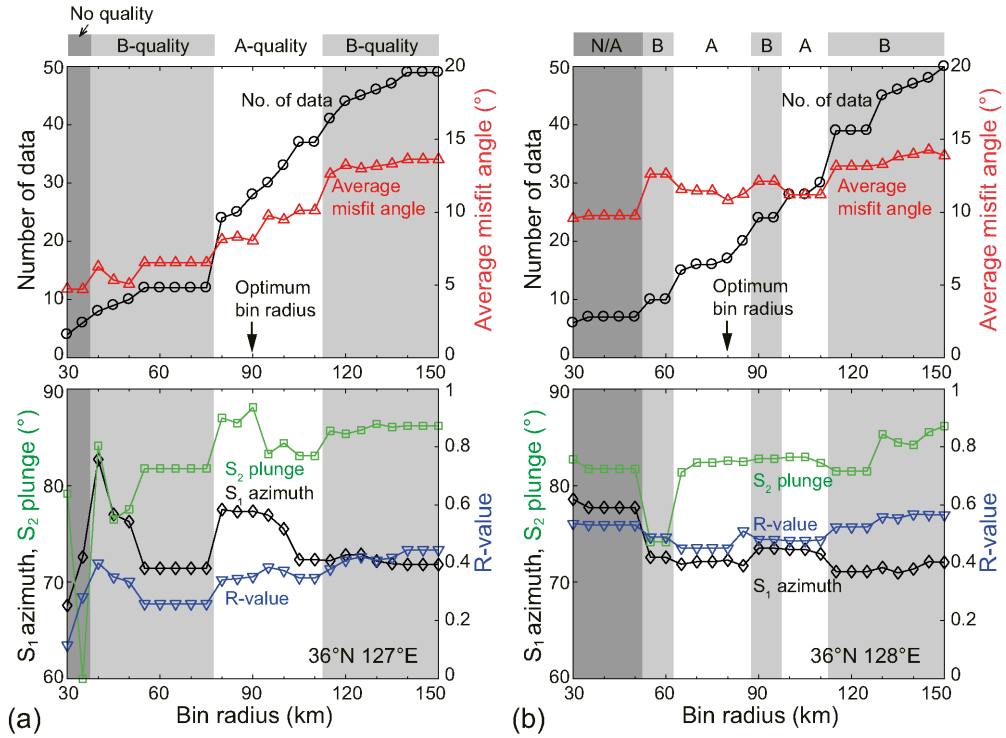

Figure 3. Plots showing number of data points and *R*-value against bin radius for grid points (a) 36° N, 127° E and (b) 36° N, 128° E. These plots show our procedure used to optimize bin size, which is designed to include the highest number of data points in the bin, while keeping the average misfit angle obtained from the inversion low. We also plot key inversion results, including the maximum principal stress (S_1) azimuth, intermediate principal stress (S_2) plunge, and *R*-value for the best-fit stress tensor.

emphasizes the importance of the number of available focal mechanism solutions for the stress inversion.

The results of our inversion (Fig. 4a) show that the confidence regions for the three principal stress orientations, especially those for the maximum principal stress (S_1), are generally well constrained at individual grid points and fairly consistent over the country. The best-fit orientations of S_1 are almost horizontal (average plunge of 5°) and oriented ENE–WSW, with an average azimuth of N73° E; however, there is a ~40° spread in the S_1 azimuth depending on locations. The confidence regions show that the intermediate principal stresses (S_2) are consistently sub-vertical over the peninsula, without clear variation from region to region. The confidence intervals for S_2 and S_3 in east offshore exhibit long and narrow plunge dispersions along the plane perpendicular to the S_1. This alludes that the magnitudes of S_2 and S_3 in east offshore may be close to each other, which will be further investigated in the next section. The best-fit S_2 orientations are nearly vertical at all grid points analysed. The two maximum deviations of S_2 from vertical are at 35° N, 127° E (16°) and 37° N, 127° E (12°), where the stress inversions use only eight data points (the minimum number of data points needed to qualify for a B-quality classification). At all other locations the plunge of S_2 is within 10° of vertical; the calculated plunge is nearer vertical for A-quality stress data (average plunge of 86° ± 2°) than for B-quality data (average plunge of 83° ± 4°). We infer that our inversion would yield a vertical intermediate principal stress if a larger number of focal mechanism solutions were available. Thus, the prevailing stress regime favours strike-slip faulting throughout the country. Since there is no significant change in the orientation of stress across the study area, we also run the inversion without binning the data, and inverting all data points at once. This inversion produces a misfit angle of 14.6°, giving it a B-quality ranking, and yields an S_1 azimuth of N74° E and a vertical (90°) S_2. It should be noted that the higher misfit angles at some locations, resulting in B-quality inversion results for some grid points, indicate a small amount of spatial variability in the stress orientations. In general, however, there is a fairly consistent orientation of the stress field at seismogenic depths in and around the Korean Peninsula.

The stress results in Fig. 4(a) are obtained from inversion of preferred fault planes that would minimize the average misfit angles. This method provides a statistical degree of homogeneity in stress field in terms of misfit angle. However, some recent studies demonstrate that the use of misfit angle to determine preferred fault planes may not necessarily be accurate based on some synthetic tests on known fault planes a priori (Vavryčuk 2014; Martínez-Garzón *et al.* 2016). Vavryčuk (2014) used a parameter defining instability to select the preferred fault having higher instability out of the two nodal planes in each focal mechanism, and demonstrated that this method gives a better prediction of correct fault planes. Since resulting stress tensors may differ depending on which nodal planes are inverted, we also run stress inversion using the instability method for the same data set used for the misfit angle method above. The results of this inversion are shown in Fig. 4(b). Although some fault planes are selected differently from the misfit angle method, the results are generally analogous to those in Fig. 4(a). The S_1 confidence regions at all grid points are quite well constrained in horizontal orientations. The best-fit S_1 azimuths are similar to those determined from the misfit angle method, with their average difference of less than 5°. The orientations of S_2 are near vertical in most of grid points, although there are some dispersions of S_2 confidence regions in some locations. Two exceptions are found at 35° N, 125° E and 35° N, 127° E, where the plunges of the best-fit S_2 deviate significantly from vertical (by 76° and 54°, respectively). In these regions, the

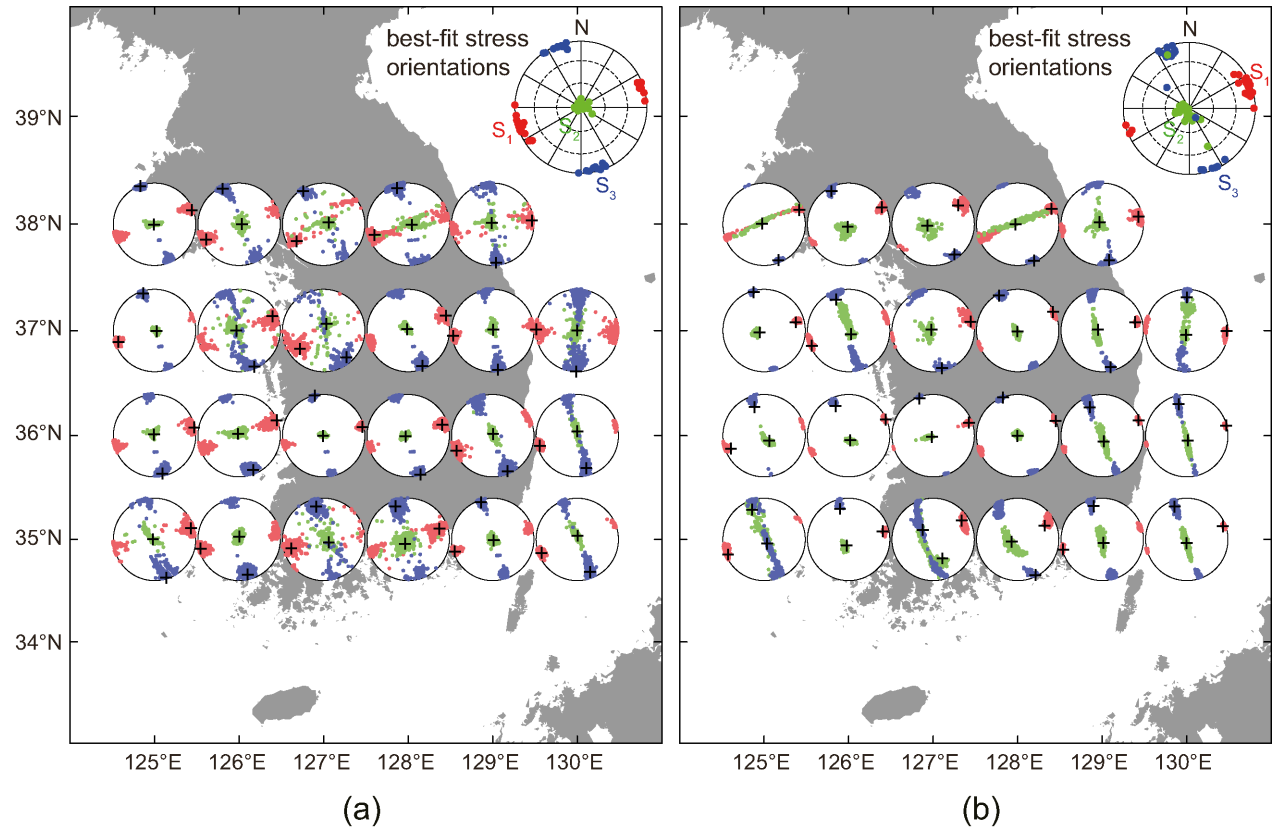

Figure 4. Results of stress inversions. Two approaches are used to select preferred fault planes: (a) using misfit angle method and (b) using instability method. At each grid point, 95 per cent confidence intervals for the three principal stresses are marked using red (S_1), green (S_2) and blue (S_3) colours in lower hemisphere stereonet, which are derived using bootstrap resampling of the selected fault planes. The corresponding best-fit stress orientations are marked as plus (+) symbols. The best-fit stress orientations are also plotted in inset stereonets.

number of focal mechanism solutions inverted is only 8; thus, using some fault planes selected differently could cause a significant difference in stress results. More focal mechanism data may be needed to elucidate stress states in these regions. Overall, the two inversion results using the misfit angle method and the instability method show fairly consistent stress orientations at seismogenic depths in and around the Korean Peninsula.

A noteworthy feature of our gridded stress inversion procedure is that it enables us to observe a systematic spatial variation of the *R*-value (Fig. 5). This pattern cannot be observed in a simple stress orientation map, and the inversion that use all data points at once, without separating them into bins, only gives an average *R*-value over the entire region. *R*-value is known to be difficult to constrain when the number of inverted focal mechanism data is small, and especially if fault planes are wrongly selected (Vavryčuk 2014). Our inversions from bootstrap resampling of the sets of faults using the two different techniques (Figs 5a and b, respectively) yield relatively well constrained *R*-value distributions. Standard deviations of *R*-value distributions derived from the misfit angle method range between 0.04 and 0.17 (Fig. 5a). The same measures derived from the instability method are even narrower ranging between 0.03 and 0.11 (Fig. 5b). In Fig. 6, we compare the *R*-values derived from the two inversion methods. Although the two sets of *R*-values from the respective methods are not often comparable each other with the maximum difference as high as 0.36, there is a general consistency between them such that if an *R*-value is low (or high) from a method, so is it from the other method. The best-fit *R*-value derived from the misfit angle method varies between 0.13 and 0.75 depending on locations, whereas that from the instability method varies more contrastingly between 0.11 and 0.89. Generally, the instability method appears to result in *R*-values more sensitively depending on locations than the misfit angle method. Without clearly knowing actual fault planes at depth from our double-couple fault mechanism data, we are not sure of which method provides more accurate *R*-values. However, based on the previous synthetic studies by Vavryčuk (2014) and Martínez-Garzón (2016), we assume that the instability method be more accurate in calculating *R*-values, and will describe *R*-value variation based on results from the instability method.

We find that there is resolvable spatial variation in *R*-value with locations. The *R*-values are highest in the east (in a range between 0.81 and 0.89), reflecting the dense distribution of reverse faulting mechanisms in that region. A relatively low *R*-value (0.22) is obtained offshore to the northwest, where normal faulting events are clustered. Since the *R*-value indicates the relative magnitude of S_2 within the maximum differential stress ($S_1 - S_3$) range, this information provides an opportunity to estimate the magnitudes of the stresses if we have some additional quantity about the maximum differential stress.

4 ESTIMATING STRESS MAGNITUDES

Our stress magnitude estimation is applied to the locations where the stress states are strike-slip faulting stress regime, in which the intermediate principal stress S_2 is close to vertical. Such areas cover almost the entire country except for two locations. Based on our

Table 2. Summary of stress inversion results.

Lat (°)	Lon (°)	Bin radius (km)	Number of data points	Average misfit angle (°)	S_1 azimuth (°)	S_1 plunge (°)	S_2 plunge (°) (°)	WSM rank	Stress regime	R
38	125	80	16	7.0	69	2	88	A	SS	0.29 ± 0.07
					68	5	84		SS	0.22 ± 0.04
38	126	105	12	11.0	65	7	82	B	SS	0.52 ± 0.09
					63	6	82		SS	0.45 ± 0.05
38	127	110	8	10.3	57	7	83	B	SS	0.48 ± 0.12
					53	16	73		SS	0.53 ± 0.06
38	128	125	10	8.1	72	9	80	B	SS	0.13 ± 0.13
					66	6	84		SS	0.11 ± 0.08
38	129	130	8	6.2	85	3	86	B	SS	0.57 ± 0.15
					79	6	81		SS	0.68 ± 0.07
37	125	90	17	7.6	73	5	84	A	SS	0.45 ± 0.08
					75	13	77		SS	0.68 ± 0.05
37	126	65	8	11.5	67	7	82	B	SS	0.50 ± 0.16
					67	2	61		SS	0.78 ± 0.08
37	127	85	8	6.3	55	12	78	B	SS	0.44 ± 0.17
					76	4	64		SS	0.70 ± 0.07
37	128	105	19	9.3	68	1	86	A	SS	0.62 ± 0.13
					63	2	87		SS	0.76 ± 0.05
37	129	90	17	10.4	83	2	87	A	SS	0.61 ± 0.10
					79	12	78		SS	0.76 ± 0.05
37	130	70	9	16.5	92	0	90	B	SS	0.73 ± 0.14
					88	10	78		SS	0.81 ± 0.08
36	125	110	21	12.0	78	1	84	B	SS	0.46 ± 0.09
					69	8	70		SS	0.65 ± 0.04
36	126	75	18	14.5	68	1	84	B	SS	0.34 ± 0.07
					66	1	76		SS	0.64 ± 0.04
36	127	90	28	8.0	77	2	88	A	SS	0.35 ± 0.04
					70	5	85		SS	0.41 ± 0.06
36	128	80	17	10.8	72	7	83	A	SS	0.45 ± 0.09
					69	1	89		SS	0.65 ± 0.03
36	129	70	20	15.2	67	3	85	B	SS	0.64 ± 0.09
					67	3	74		SS	0.84 ± 0.04
36	130	100	32	18.6	75	2	86	B	SS	0.75 ± 0.09
					76	1	48		SS	0.86 ± 0.03
35	125	75	8	7.4	73	4	85	B	SS	0.56 ± 0.13
					67	3	14		TF	0.79 ± 0.06
35	126	135	22	17.4	77	2	82	B	SS	0.43 ± 0.07
					77	9	73		SS	0.79 ± 0.03
35	127	90	8	15.4	75	12	74	B	SS	0.58 ± 0.12
					56	10	36		TF	0.84 ± 0.11
35	128	90	8	11.2	69	5	84	B	SS	0.49 ± 0.12
					63	17	72		SS	0.56 ± 0.08
35	129	95	16	10.2	72	2	86	A	SS	0.63 ± 0.06
					75	1	63		SS	0.81 ± 0.04
35	130	120	26	16.8	69	4	80	B	SS	0.73 ± 0.09
					70	4	80		SS	0.89 ± 0.04
All-inclusive inversion			152	14.6	74	0.3	89.6	B	SS	0.51 ± 0.15
					70	6	74		SS	0.66 ± 0.20

Note: In each raw, the upper values are from the misfit angle method and the lower values are from the instability method.

inversion results, we assume that S_2 is the vertical stress (S_v) and that the other two principal stresses (S_1 and S_3) acting in the horizontal plane are the maximum and minimum horizontal principal stresses (S_{Hmax} and S_{hmin}), respectively. The R-value is then defined as

$$R = \frac{S_{Hmax} - S_v}{S_{Hmax} - S_{hmin}} \quad (1)$$

and gives the relative magnitude of S_v within the differential horizontal stress ($S_{Hmax} - S_{hmin}$). To estimate the magnitudes of the three individual principal stress components, we require two additional independent constraints. We use a method similar to that described by Zoback (1992) and Plenefisch & Bonjer (1997), as follows.

One assumption is that the vertical stress, S_v, is lithostatic, and can be estimated independently from the weight of the overburden. For example, if we use a typical unit weight of granitic rocks for continental crust (26.5 kN m^{-3}), S_v is estimated to be 26.5z MPa, where z is depth in km. Fig. 7 shows a Mohr diagram that graphically illustrates our procedure used to estimate the stress magnitudes. We assume that pore pressure (P) is hydrostatic in the brittle crust (Zoback & Townend 2001). The Mohr circle, which represents the directional variation of the shear stress, τ, and the normal stress, σ, will move left or right depending on the R-value. The vertical effective stress ($S_v - P$) is fixed; thus, the diagram provides information about the relative magnitudes of the two horizontal principal

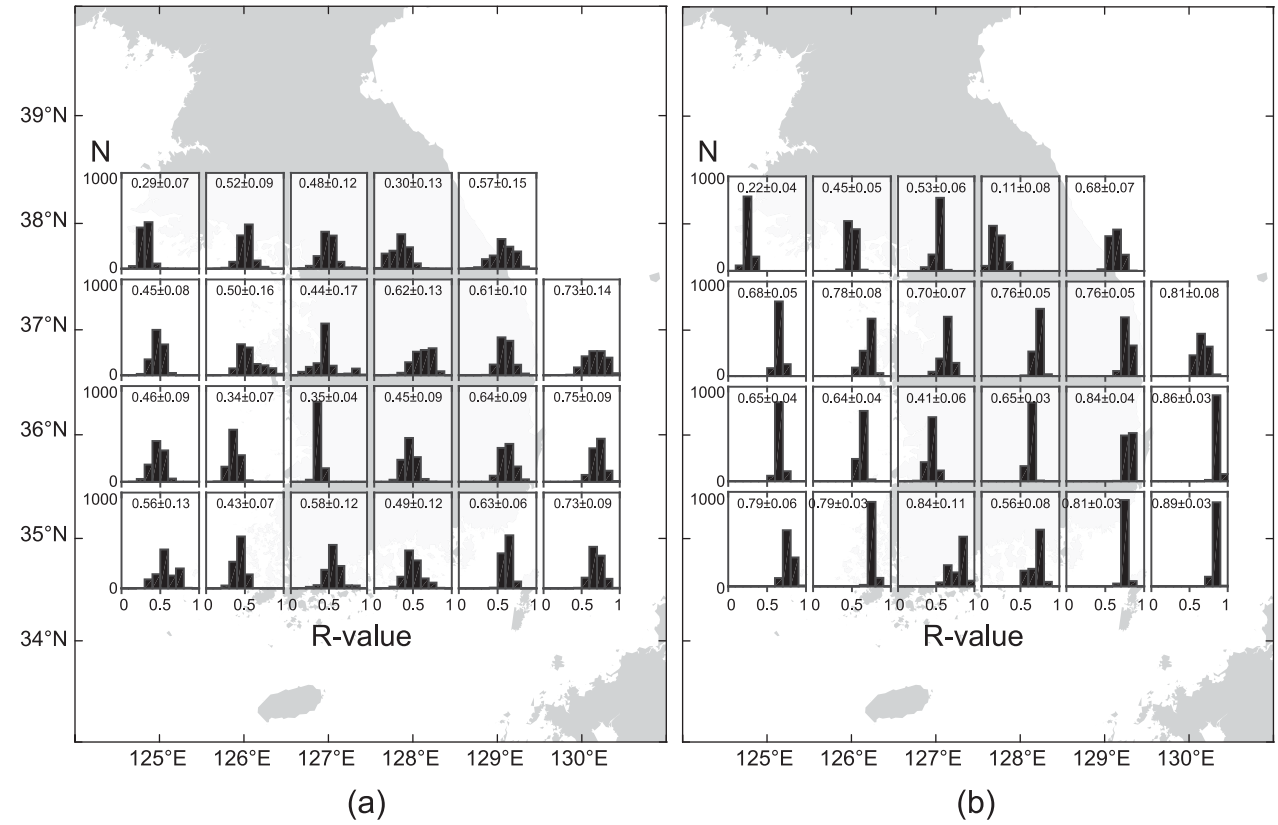

Figure 5. Histograms of R-value at individual grid points, derived using (a) misfit angle method and (b) instability method. The best-fit R-value and standard deviation are indicated in each histogram.

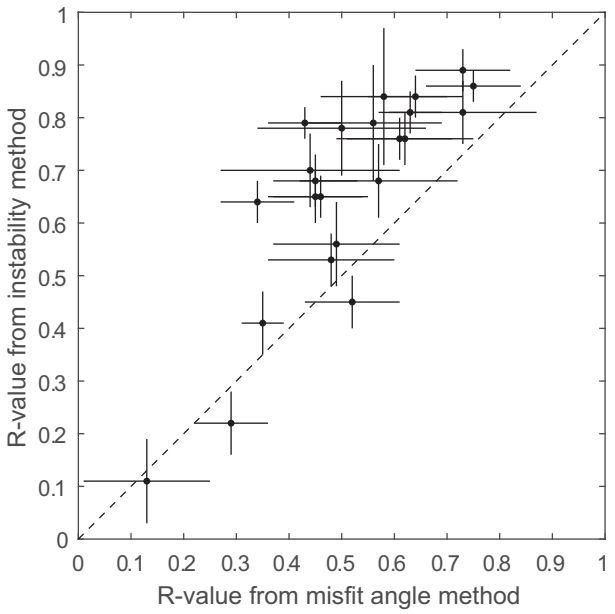

Figure 6. Comparison of R-values derived from instability method and misfit angle method. Horizontal and vertical lines indicate standard deviations of R-values. The dashed diagonal line denotes the condition where R-values from the two methods are identical.

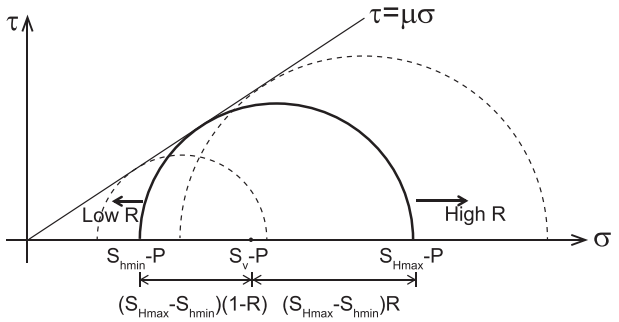

Figure 7. The effect of R-value on Mohr circles. A Mohr circle is a graphical expression of the stress state on a fault, plotted on a diagram of shear (τ) versus effective normal stress (σ). The effective normal stress is the total normal stress minus pore pressure, P. The diameter of the circle represents the maximum differential stress ($S_{\mathrm{Hmax}} - S_{\mathrm{hmin}}$) and is limited by the friction (μ) on the fault that is best oriented for slip under a given stress condition. Thus, the circle should lie below the Coulomb frictional criterion ($\tau = \mu\sigma$). For a fixed effective vertical stress ($S_{\mathrm{v}} - P$), the position of the Mohr circle moves laterally depending on the R-value. This allows us to estimate the two horizontal principal stresses in a strike-slip regime.

stresses. To estimate the absolute magnitudes of the two horizontal principal stresses, we assume that the maximum differential stress, $S_{\mathrm{Hmax}} - S_{\mathrm{hmin}}$ (equivalent to the diameter of the Mohr circle) is limited by friction (μ) on optimally oriented faults (Sibson 1974), which is expressed by the Coulomb friction law, $\tau = \mu\sigma$. This stress constraint scales the size of the Mohr circle such that the maximum differential stress increases as the R-value rises, thus enabling us to estimate the absolute magnitudes of horizontal principal stresses. This second constraint on the stress condition is reasonable since earthquakes are ubiquitous over the Korean Peninsula, and any excessive differential stress would be released by slip along optimally oriented fault planes.

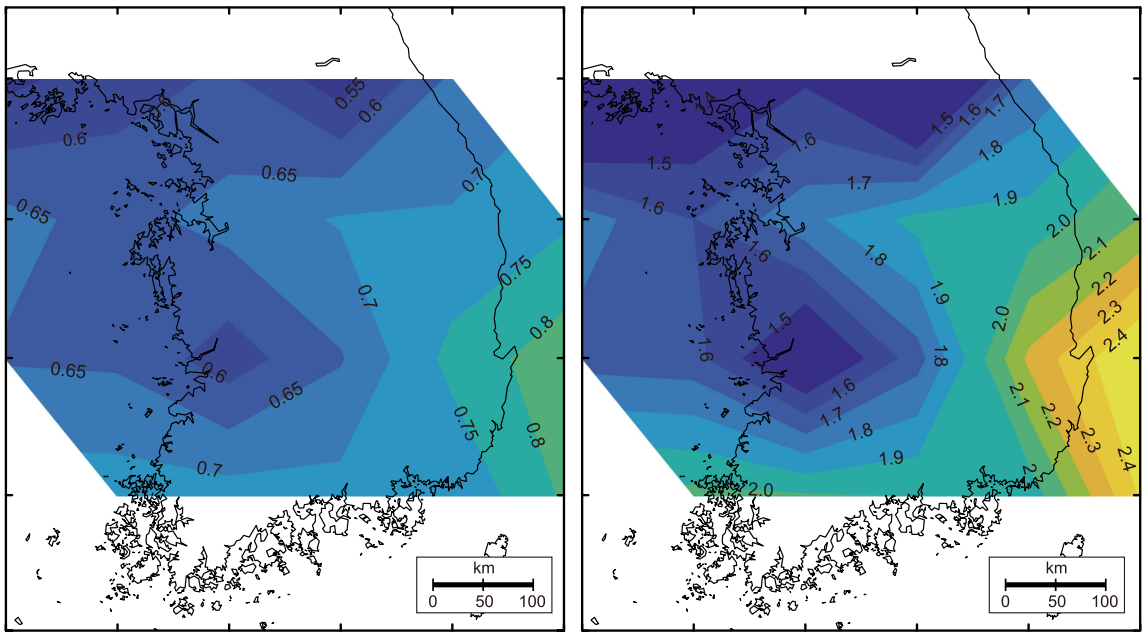

Figure 8. Spatial variations in (a) the minimum ($S_{\rm hmin}$) and (b) maximum horizontal principal stress ($S_{\rm Hmax}$). $S_{\rm hmin}$ and $S_{\rm Hmax}$ have been normalized by the vertical stress ($S_{\rm v}$), and both show an eastward increase in magnitude.

Our calculation of the magnitudes of the stress can be expressed analytically as follows. The Coulomb friction law can be rewritten in terms of the principal stresses (Jaeger *et al.* 2009):

$$S_{\rm Hmax} - P = \left(\sqrt{\mu^2+1}+\mu\right)^2 (S_{\rm hmin} - P). \tag{2}$$

Combining eqs (1) and (2), it is straightforward to derive the horizontal principal stresses normalized by vertical stress:

$$S_{\rm hmin}/S_{\rm v} = \frac{1}{1-(1-R)\left(1-\left(\sqrt{\mu^2+1}+\mu\right)^2\right)}\left(1-\frac{P}{S_{\rm v}}\right) + \frac{P}{S_{\rm v}} \tag{3a}$$

$$S_{\rm Hmax}/S_{\rm v} = \frac{\left(\sqrt{\mu^2+1}+\mu\right)^2}{1-(1-R)\left(1-\left(\sqrt{\mu^2+1}+\mu\right)^2\right)}\left(1-\frac{P}{S_{\rm v}}\right) + \frac{P}{S_{\rm v}} \tag{3b}$$

where the ratio of $P/S_{\rm v}$ is ~0.37 for the condition of hydrostatic pore pressure. We assume the frictional coefficient on faults, μ, based on Byerlee's law (Byerlee 1978): at effective normal stresses below 200 MPa, the maximum friction that must be overcome for a fault to slip lies in the range 0.6–1.0, with an average of 0.85, whereas μ is ~0.6 at effective normal stresses greater than 200 MPa. Based on the magnitude of $S_{\rm v}$ at seimsogenic depths, we estimate that the effective normal stresses are less than 200 MPa. Thus, we use a value of $\mu = 0.85$ for the reference frictional coefficient on optimally oriented faults. It should be noted that the stress magnitude calculation will yield different results depending on the assumed μ value. Other studies have assumed different reference μ values for the calculation of stress magnitudes (e.g. ~0.65; Zoback 1992; Plenefisch & Bonjer 1997). We will discuss the issues related to the assumed reference μ value in detail later.

We calculate the values of $S_{\rm Hmax}/S_{\rm v}$ and $S_{\rm hmin}/S_{\rm v}$ at each grid point using the R-value and the assumed constant μ, and then interpolate between grid points. Our results are shown in Fig. 8. The magnitudes of the horizontal stresses increase eastward. The value of $S_{\rm Hmax}/S_{\rm v}$ increases rapidly from 1.9 to 2.4 in eastern Korea, while it is generally stable at around 1.5–1.8 in the west. The ratio of $S_{\rm hmin}/S_{\rm v}$ also increases eastward, but more gradually, from 0.6 to 0.8. It is worth reiterating that the absolute values of $S_{\rm Hmax}/S_{\rm v}$ and $S_{\rm hmin}/S_{\rm v}$ are dependent on the value of the frictional coefficient. For example, if we assume a higher μ value, the values of $S_{\rm Hmax}/S_{\rm v}$ and $S_{\rm hmin}/S_{\rm v}$ would increase accordingly.

It is worth considering whether the variation we observe in the magnitudes of the horizontal stress is real, or whether it is an artefact due to our assumption of a constant frictional coefficient. If we accept that the frictional coefficient is likely to vary between different faults, and assume that μ is higher on faults in the west (low-stress) compared with the east (high-stress), it may be possible to generate a stress magnitude map with a uniform stress magnitude. To test this possibility, we investigate the sensitivity of the stress ratios to the R-value ($0.11 < R < 0.89$) and Byerlee's frictional coefficient ($0.6 < \mu < 1.0$). In Fig. 9 the stress ratio contour lines are almost parallel to the μ axis, showing that $S_{\rm Hmax}/S_{\rm v}$ is more sensitive to the R-value than to μ. For a given R-value, a change in μ from 0.85 to 0.65 results in a decrease in the $S_{\rm Hmax}/S_{\rm v}$ value of only ~0.1, which is small compared with the whole range of $S_{\rm Hmax}/S_{\rm v}$ values shown in Fig. 8. In other words, the first-order pattern of stress variations is relatively insensitive to the value of μ. This implies that the spatial variation of the horizontal stress magnitudes that we describe is real, although a slight change in absolute values of horizontal stresses is possible depending on actual frictional coefficients and R-values within standard deviation.

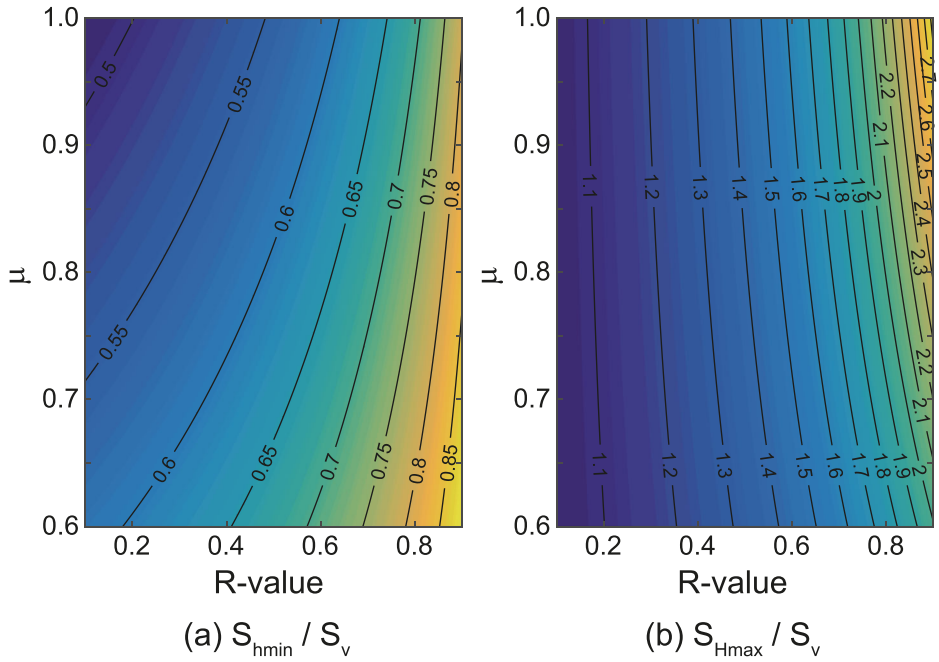

Figure 9. Variations in (a) $S_{\rm hmin}/S_{\rm v}$ and (b) $S_{\rm Hmax}/S_{\rm v}$ as a function of the frictional coefficient (μ) and R-value. Note that the $S_{\rm Hmax}/S_{\rm v}$ value depends primarily on the R-value, and is less sensitive to the frictional coefficient.

5 FRICTIONAL COEFFICIENTS OF FAULTS

One of the constraints we used to estimate horizontal stress magnitudes is that there is frictional equilibrium between stress and friction along optimally oriented faults (eq. 2). This constraint limits the maximum differential stress, which is ($S_{\rm Hmax} - S_{\rm hmin}$) in a strike-slip regime, such that any excessively large differential stresses are released by slip along the most critically oriented faults. In a strike-slip faulting stress regime, the critical faults have vertical dips and strike at $\sim$40° ($\tan^{-1}\mu$) from the $S_{\rm Hmax}$ azimuth (Jaeger *et al.* 2009). In reality, however, almost all the focal planes used in our study deviate somewhat from the ideal orientation, especially for the normal and reverse faulting events. In other words, the stress conditions resolved on the actual fault planes are not high enough to cause slip if the frictional coefficient is 0.85. Since the occurrence of earthquakes proves that the faults did slip, the frictional coefficient on the faults must be lower than for the ideal, optimally oriented fault.

To estimate the range of values for the frictional coefficient over which faults can slip, we calculate the shear stress (τ) and effective normal stress (σ) acting on individual faults under a given stress state. For fault slip to occur, τ should exceed (or be approximately equal to) the slip-resisting stress defined by $\mu\sigma$, from which we can evaluate the frictional coefficient. Fig. 10 shows the calculated ranges of frictional coefficient. The upper limit (0.85) corresponds to the ideal case where the fault is optimally oriented for slip under a given stress state. The average frictional coefficient of all faults (0.71 ± 0.07) is somewhat lower than the ideal case since the actual fault planes deviate from the ideal orientation. Different fault types have distinct frictional coefficients. The faults that slipped in a strike-slip sense have the highest frictional coefficients, with a mean value of 0.75 ± 0.04, since they are oriented close to the ideal case. For normal faulting events, the average frictional coefficient is 0.66 ± 0.07, and for the reverse faulting it is even lower, at 0.59 ± 0.06. It should be noted that our results do not necessarily indicate that different types of fault have intrinsically different

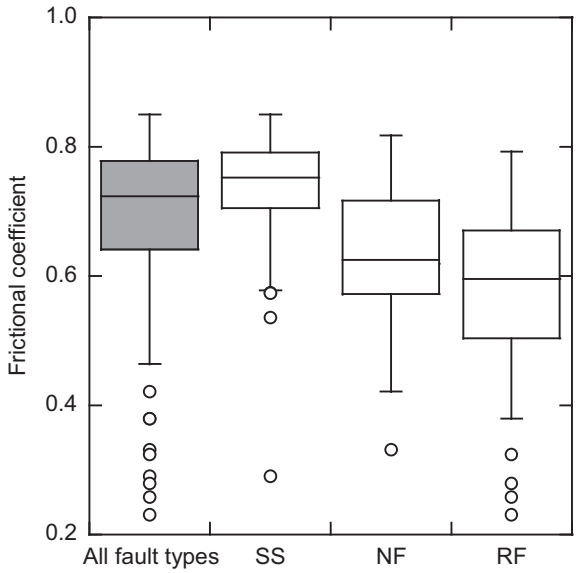

Figure 10. Estimates of the range of frictional coefficients for different types of fault. Most faults have frictional coefficients between 0.6 and 0.8. Based on our estimates, different faulting types have slightly different ranges of frictional coefficient; that is, strike-slip faults (SS) have the highest values, followed by normal (NF) and reverse (RF) faults. Circles denote outliers.

frictional properties. The friction on faults is known to be affected by various factors, but primarily by the composition of fault gouge material (e.g. Morrow *et al.* 2000; Takahashi *et al.* 2007). There is no reason that a particular type of fault should have frictional properties different to those of other types of fault. There may also exist faults with a very high coefficient of friction that are strong enough to sustain the current stress condition without failing; however, these are not relevant to our study. The normal and reverse faults analysed in this study, which slipped under a strike-slip stress

regime, failed because they have lower frictional coefficients than the ideal case.

Our evaluation of frictional coefficients is based on our initial assumption that the frictional coefficient of the most critically oriented fault is 0.85. It can be argued that Byerlee's law describes the frictional limits on a fault plane regardless of its orientation, and can, therefore, be applied to faults that do not lie in the optimal orientation for slip, especially because they are the faults that will limit the stress condition in the crust. In fact, the conceptual, most optimally oriented faults do not exist in our data. Our results indicate that most faults have frictional coefficients of 0.6–0.8 (Fig. 10), which is well within the Byerlee's range, although some have exceptionally low frictional coefficients. If we use a lower reference value for the frictional coefficient for optimally oriented faults, the resulting frictional coefficients for the faults that actually slipped will be even lower. Thus, the initial assumption of $\mu = 0.85$ for optimally oriented faults is reasonable.

6 DISCUSSION

6.1 Different faulting types in different regions

Strike-slip faulting is the most favourable type given the stress field in the Korean Peninsula. We can now also explain the other faulting styles observed offshore to the northwest (normal faulting) and on the east coast (reverse faulting) in terms of the difference in the magnitudes of tectonic stresses. Several normal faulting events occurred along faults striking subparallel to the maximum horizontal principal stress direction and dipping in the direction of the minimum horizontal stress (Fig. 11a). The occurrence of normal faulting events is consistent with the relatively low horizontal stresses in that region (Fig. 11a). The reverse faulting events ($M = 2.7$–5.3) clustered off the east coast (Fig. 11b) are interpreted to result from the reactivation of normal faults; that is, the Ulleung Fault and Hupo Fault (Yoon *et al.* 1997; Kang & Baag 2004; Choi *et al.* 2012). Although the strikes of the faults are somewhat variable, the fault planes generally dip eastward at 28°–59°. The reactivation of normal faults (which generally have a steeper dip than typical thrust faults) in a reverse sense requires high horizontal stresses, consistent with the stress magnitudes that we obtained for that region.

To quantitatively evaluate the mechanics of faulting in the Korean Peninsula, we calculate the shear and effective normal stress acting on our preferred fault planes and plot them on a Mohr diagram (Fig. 11c). Note that we normalize the stresses by S_v. In the NW, where tectonic stresses are relatively low, the shear (τ) and effective normal stress (σ) resolved on the fault planes indicate that the faults are oriented such that they exhibit a relatively high slip tendency (τ/σ) for the given stress state in that region. As expected, faults that moved in a strike-slip sense exhibit the highest slip tendency (0.7–0.8). Those activated in a normal sense also exhibit a relatively high slip tendency (~0.6–0.7) for the stress field. To investigate whether the observed low state of tectonic stress is a pre-requisite for the normal faulting, we examine how slip tendency varies with the magnitude of tectonic stress, represented by the R-value (Fig. 11e). Note that the range of slip tendency shown in Fig. 11e is due to the slight attitude variations between individual fault planes. The strike-slip faults always exhibit the highest slip tendency, maintaining values of 0.7–0.8 regardless of R-value. The slip tendency of normal faults decreases with increasing R-value (and increasing magnitude of tectonic stress). If we assume that the frictional coefficient of the normal faults is 0.66 ± 0.07, as estimated above, the R-value that can activate the faults should be lower than ~0.4. If the R-value is higher than 0.4, some faults would not have been activated, as the slip tendency would be below the lower limit of the frictional coefficient. Thus. a low tectonic stress state is a necessary condition for normal faulting in this region.

In the east coast region, the slip tendency of the reverse faults ranges widely between 0.6 and 0.8 (Fig. 11d) because of the variable orientations of the fault planes. If we assume that the frictional coefficients of these faults are within 0.59 ± 0.06, the values of slip tendency are within or higher than the frictional coefficient range, which allows the faults to slip. To evaluate whether a high tectonic stress is necessary to trigger reverse faulting in this region, we calculate the slip tendency for a range of R-values. The slip tendency of reverse faults increases with the R-value (Fig. 11f); a high R-value is thus favourable for reverse slip. If the R-value is lower than ~0.8, some of faults would have a slip tendency below the lower limit of frictional coefficient, meaning they could not slip unless their frictional coefficient is unrealistically low. Therefore, we conclude that a high tectonic stress is necessary to induce reverse slip in this region.

6.2 Possible cause of heterogeneity in stress magnitude

While the stress orientations are fairly consistent in and around the Korean Peninsula, the stress magnitudes vary significantly. The magnitudes tend to increase towards the east, and this pattern is most intense in eastern Korea, where the increase in the S_{Hmax}/S_v ratio is approximately 0.4/100 km (Fig. 8). This rate corresponds to a horizontal gradient of S_{Hmax} as high as ~120 MPa/100 km at the average seismogenic depth (11 km). Below, we discuss the possible causes of the variation in the magnitude of stresses in east Korea.

Small-scale (reservoir) variations in stress magnitudes can be explained by various factors such as pore pressure heterogeneity (e.g. Yassir & Rogers 1993; Grauls & Baleix 1994), changes in fracture networks (e.g. Evans *et al.* 1989; Chang *et al.* 2010), and variations in the mechanical properties of rock (e.g. Evans *et al.* 1989). The regional-scale tectonic stress heterogeneity observed in our study may be attributable to a much larger-scale variation in the mechanical properties of the crust. In fact, ocean-bottom seismic surveys reveal that east Korea can be divided into two main crustal structures: continental crust onshore and oceanic crust offshore to the east (Cho *et al.* 2004). The boundary between continental and oceanic crusts is lies slightly east of the coast and runs subparallel to the coastline. The seismic and geophysical surveys show a distinct contrast in the physical properties of the granitic continental crust compared with the basaltic oceanic crust (Kim *et al.* 2003; Cho *et al.* 2004). Since stresses are transmitted through the crust, the properties of the crust will have a direct effect on the transfer of stress.

To demonstrate property-controlled stress transfer, we simulate the crustal stress distribution around east Korea using a finite element method, assuming that the crust behaves as a linear elastic material. We employ a simple 2-D layered model as proposed by Cho *et al.* (2004) based on their geophysical survey (Fig. 12a). The key property that is thought to control stress transfer is the rigidity of the rock (Evans *et al.* 1989), which can be represented by Young's modulus (E). We assume typical ranges of Young's moduli for continental (50–70 GPa) and oceanic (80–100 GPa) crust, based on the published data of Watts & Ryan (1976) and Carlson & Raskin (1984). We use a simple numerical modelling setup and do not incorporate any complicated rheological layering in our model,

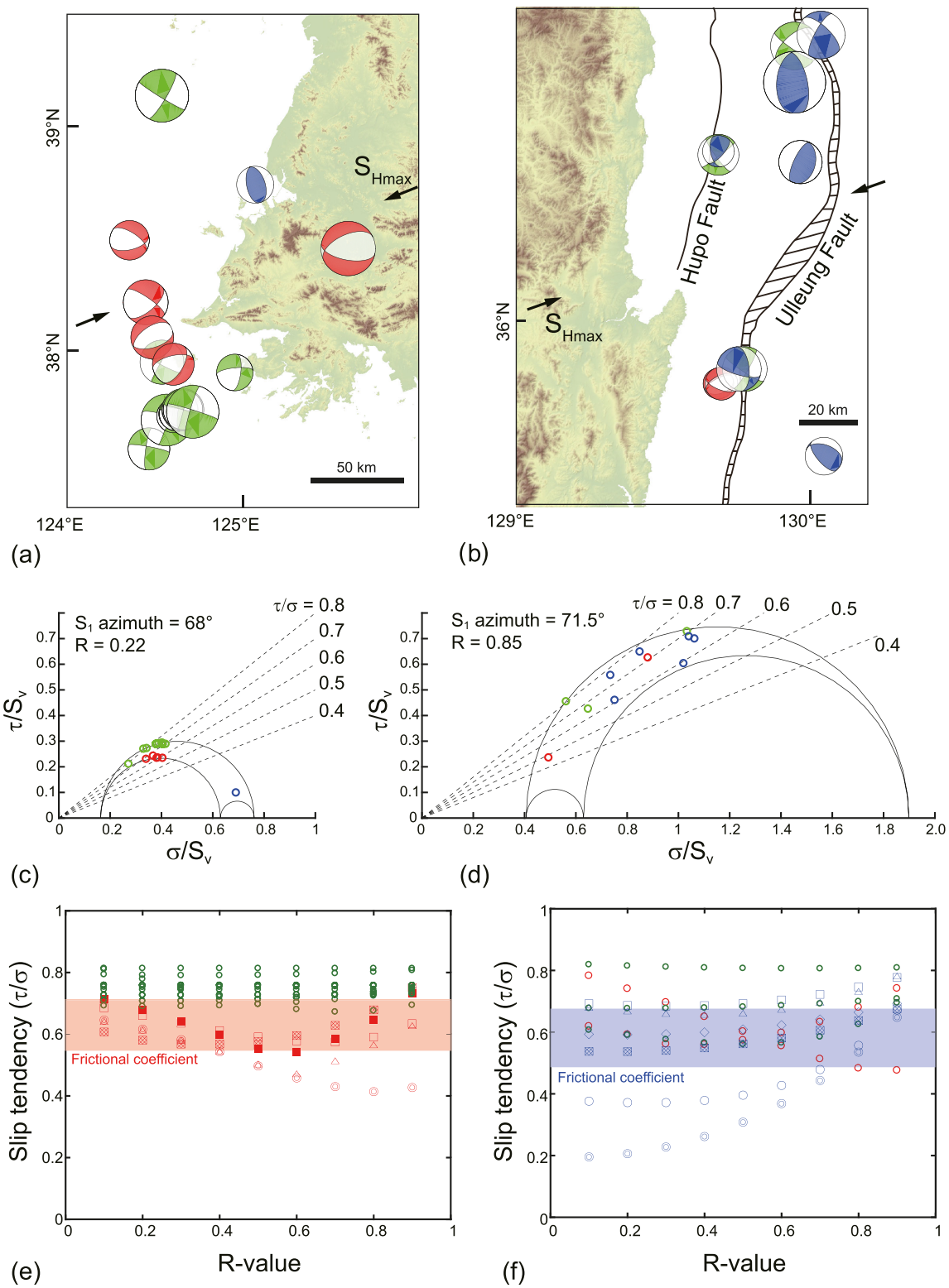

Figure 11. Comparison of the seismicity and fault mechanics of the northwestern (left-hand column) and eastern (right-hand column) offshore regions of the Korean Peninsula. LEFT: The northwestern offshore area is characterized by normal faulting (a) and the lowest *R*-value (0.22) (c). The slip tendency (τ/σ) of these faults is 0.6–0.7, which is sufficient to overcome the friction on the faults (c). If the *R*-value was high (>0.4), some of faults would exhibit a slip tendency lower than the frictional coefficient, which means that the faults would not slip. Therefore, a low *R*-value (equivalent to a low tectonic stress) is necessary to trigger normal-faulting earthquakes in this area. RIGHT: The east coast region is characterized by reverse faulting (b) and the highest *R*-value (0.85) (d). The fault slip tendency is 0.6–0.8 (d). If the *R*-value was lower (<0.8), the slip tendency of some reverse faults would be lower than the frictional coefficient (f). Therefore, a high *R*-value (high tectonic stress) is required to trigger reverse slip along the faults.

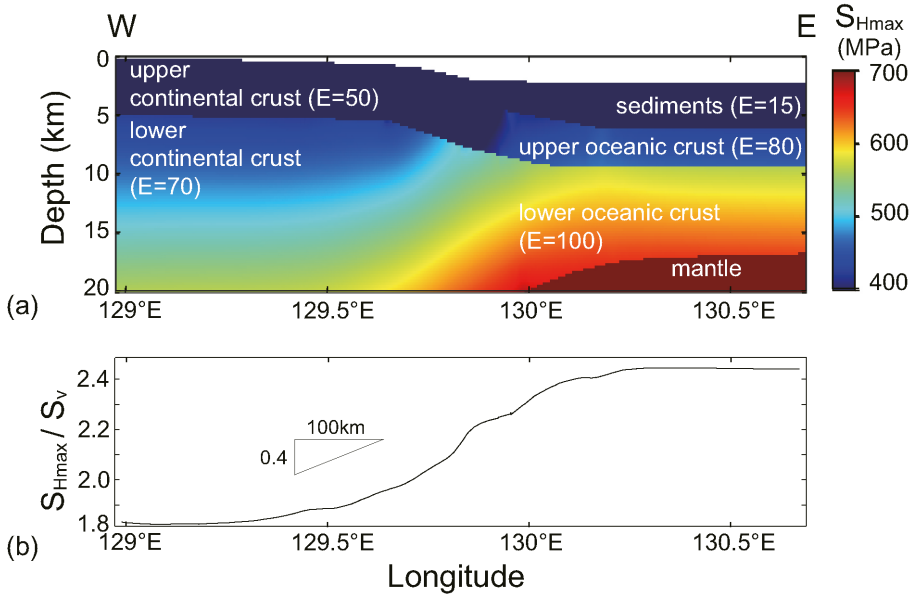

Figure 12. Results of our numerical model. (a) Variation in the magnitude of the horizontal stress as a function of depth, for continental and oceanic crust. The values of the Young's moduli (E) used in our modelling are given in GPa. The layered model is after Cho *et al*. (2004). The S_{Hmax}/S_v ratio in (b) modelled at the average focal depth (11.2 km) increases gradually eastward at a rate comparable to that (0.4/100 km) estimated in Fig. 8.

in order to gain an insight into the primary cause of stress heterogeneity. We apply a simple boundary condition of constant lateral displacement, which results in stress magnitudes similar to those shown in Fig. 8. Fig. 12(a) shows the modelled horizontal stress magnitudes (denoted by colour), which approximately correspond to S_{Hmax}. As expected, the modelled horizontal stress magnitudes vary significantly with the rigidity of the rock, such that for higher rigidities there are higher magnitudes of stress. There is a clear transition from low to high stresses across the boundary between continental and oceanic crust. At the average earthquake focal depth (∼11 km), the modelled S_{Hmax}/S_v ratio changes from ∼1.8 in continental crust to ∼2.4 in oceanic crust (Fig. 12b). The transition rate is slightly higher than, but comparable to, that estimated in Fig. 8 (0.4/100 km). Therefore, our modelling suggests that the high stresses to the east of the Korean Peninsula may be attributed to the presence of stiff oceanic crust.

7 CONCLUSIONS

We used 152 well-constrained focal mechanism solutions for $2.5 \leq M \leq 5.8$ earthquakes that occurred between 1976 and 2016 in and around the Korean Peninsula, to characterize the tectonic stress state in this region. To tackle the uncertainty in stress field due to the ambiguity in correct fault planes from double-couple focal mechanism solutions, we use two different approaches in selecting preferred fault planes. In the first approach, we derive the most reliable stress inversion results for our data set by optimizing the bin size at regularly spaced grid points, in order to invert a larger number of focal mechanism solutions while minimizing the average misfit angles between the earthquake slip vector and the modelled orientation of the maximum shear stress on the faults. Our stress inversions yield A- and B-quality results based on the WSM quality ranking scheme. In the second approach, we use the instability criterion to select and invert the preferred fault planes that exhibit higher instability out of the two nodal planes of individual focal mechanisms.

From both inversions, our estimate of the orientation of tectonic stresses suggests that the stress state generally favours a strike-slip faulting regime in the Korean Peninsula and that S_{Hmax} is oriented ENE–WSW. Although the orientations of the stresses are relatively consistent, the magnitudes of the horizontal stresses, which we deduced from the R-value, vary across the region, such that the S_{Hmax}/S_v ratio increases from 1.5 in the west to 2.4 in the east. The variation in the magnitude of tectonic stress is consistent with the observed pattern of seismicity; that is, normal faulting in the northwest, where the horizontal stress is relatively low, and reverse faulting in east, where the horizontal stress is high. We suggest that the relatively high tectonic stress in east Korea is related to the presence of stiff oceanic crust, which can transfer high magnitudes of tectonic stress.

ACKNOWLEDGEMENTS

This study was supported by the Basic Research and Development Project of the Korea Institute of Geoscience and Mineral Resources (KIGAM, Project code No. GP2015-010), funded by the Ministry of Science, ICT and Future Planning, Korea. Comments made and improvements suggested by two anonymous reviewers greatly enhanced the quality of the paper.

REFERENCES

Amato, A. & Montone, P., 1997. Present-day stress field and active tectonics in southern peninsular Italy, *Geophys. J. Int.*, **130**, 519–534.

Angelier, J., 1979. Determination of the mean principal directions of stresses for a given fault population, *Tectonophysics*, **56**, T17–T26.

Barth, A., Reinecker, J. & Heidbach, O., 2016. 3 Guidelines for the analysis of earthquake focal mechanism solutions, *Scientific Technical Report 16-01*, **15**.

Byerlee, J., 1978. Friction of rocks, *Pure appl. Geophys.*, **116**, 615–626.

Carlson, R. & Raskin, G., 1984. Density of the ocean crust, *Nature*, **311**, 555–558.

Chang, C., Lee, J.B. & Kang, T.-S., 2010. Interaction between regional stress state and faults: complementary analysis of borehole in situ stress and earthquake focal mechanism in southeastern Korea, *Tectonophysics*, **485**, 164–177.

Cho, H.M., Kim, H.J., Jou, H.T., Hong, J.K. & Baag, C.E., 2004. Transition from rifted continental to oceanic crust at the southeastern Korean margin in the East Sea (Japan Sea), *Geophys. Res. Lett.*, **31**, doi:10.1029/2003GL019107.

Choi, H., Hong, T.-K., He, X. & Baag, C.-E., 2012. Seismic evidence for reverse activation of a paleo-rifting system in the East Sea (Sea of Japan), *Tectonophysics*, **572**, 123–133.

Delvaux, D. & Barth, A. 2010. African stress pattern from formal inversion of focal mechanism data, *Tectonophysics*, **482**, 105–128.

Evans, K.F., Engelder, T. & Plumb, R.A., 1989. Appalachian Stress Study: 1. A detailed description of in situ stress variations in Devonian shales of the Appalachian Plateau, *J. geophys. Res.*, **94**, 7129–7154.

Gephart, J.W. & Forsyth, D.W., 1984. An improved method for determining the regional stress tensor using earthquake focal mechanism data: application to the San Fernando earthquake sequence, *J. geophys. Res.*, **89**, 9305–9320.

Grauls, D. & Baleix, J., 1994. Role of overpressures and in situ stresses in fault-controlled hydrocarbon migration: a case study, *Ma. Pet. Geol.*, **11**, 734–742.

Hardebeck, J.L. & Michael, A.J., 2004. Stress orientations at intermediate angles to the San Andreas Fault, California, *J. geophys. Res.*, **109**, B11303, doi:10.1029/2004JB003239.

Hardebeck, J.L. & Michael, A.J., 2006. Damped regional-scale stress inversions: methodology and examples for southern California and the Coalinga aftershock sequence, *J. geophys. Res.*, **111**, doi:10.1029/2005JB004144.

Heidbach, O., Rajabi, M., Reiter, K., Ziegler, M. & Team, WSM, 2016. *World Stress Map Database Release 2016, GFZ Data Services*, http://doi.org/10.5880/WSM.2016.001.

Hong, T.-K. & Choi, H., 2012. Seismological constraints on the collision belt between the North and South China blocks in the Yellow Sea, *Tectonophysics*, **570**, 102–113.

Hong, T.-K., Lee, J. & Houng, S.E., 2015. Long-term evolution of intraplate seismicity in stress shadows after a megathrust, *Phys. Earth planet. Inter.*, **245**, 59–70.

Hong, T.K., Lee, J., Kim, W., Hahm, I.K., Woo, N.C. & Park, S., 2017. The 12 September 2016 M_L 5.8 midcrustal earthquake in the Korean Peninsula and its seismic implications, *Geophys. Res. Lett.*, **44**, 3131–3138.

Hsu, Y.-J., Rivera, L., Wu, Y.-M., Chang, C.-H. & Kanamori, H., 2010. Spatial heterogeneity of tectonic stress and friction in the crust: new evidence from earthquake focal mechanisms in Taiwan, *Geophys. J. Int.*, **182**, 329–342.

Jaeger, J.C., Cook, N.G. & Zimmerman, R., 2009. *Fundamentals of Rock Mechanics*, John Wiley & Sons.

Jun, M.-S., 1991. Body-wave analysis for shallow intraplate earthquakes in the Korean Peninsula and Yellow Sea, *Tectonophysics*, **192**, 345–357.

Kang, T.-S. & Baag, C.-E., 2004. The 29 May 2004, M_w =5.1, offshore Uljin earthquake, Korea, *Geosci. J.*, **8**, 115–123.

Kim, H.-J., Jou, H.-T., Cho, H.-M., Bijwaard, H., Sato, T., Hong, J.-K., Yoo, H.-S. & Baag, C.-E., 2003. Crustal structure of the continental margin of Korea in the East Sea (Japan Sea) from deep seismic sounding data: evidence for rifting affected by the hotter than normal mantle, *Tectonophysics*, **364**, 25–42.

Kim, K.-H. *et al.* 2016. The 12 September 2016 Gyeongju earthquakes: 2. Temporary seismic network for monitoring aftershocks, *Geosci. J.*, **20**, 753–757.

Kim, W.Y., Choi, H. & Noh, M., 2010. The 20 January 2007 Odaesan, Korea, earthquake sequence: reactivation of a buried strike-Slip fault?, *Bull. seism. Soc. Am.*, **100**, 1120–1137.

Kim, Y., Rhie, J., Kang, T.-S., Kim, K.-H., Kim, M. & Lee, S.-J., 2016. The 12 September 2016 Gyeongju earthquakes: 1. Observation and remaining questions, *Geosci. J.*, **20**, 747–752.

Li, B., Atakan, K., Sørensen, M.B. & Havskov, J., 2015. Stress pattern of the Shanxi rift system, North China, inferred from the inversion of new focal mechanisms, *Geophys. J. Int.*, **201**, 505–527.

Martínez-Garzón, P., Ben-Zion, Y., Abolfathian, N., Kwiatek, G. & Bohnhoff, M., 2016. A refined methodology for stress inversions of earthquake focal mechanisms, *J. geophys. Res.*, **121**, 8666–8687.

Michael, A.J., 1984. Determination of stress from slip data: faults and folds, *J. geophys. Res.*, **89**, 11 517–11 526.

Michael, A.J., 1987. Use of focal mechanisms to determine stress: a control study, *J. geophys. Res.*, **92**, 357–368.

Morrow, C., Moore, D.E. & Lockner, D., 2000. The effect of mineral bond strength and adsorbed water on fault gouge frictional strength, *Geophys. Res. Lett.*, **27**, 815–818.

Park, J.-C., Kim, W., Chung, T.W., Baag, C.-E. & Ree, J.-H., 2007. Focal mechanisms of recent earthquakes in the southern Korean Peninsula, *Geophys. J. Int.*, **169**, 1103–1114.

Plenefisch, T. & Bonjer, K.-P., 1997. The stress field in the Rhine Graben area inferred from earthquake focal mechanisms and estimation of frictional parameters, *Tectonophysics*, **275**, 71–97.

Rhie, J. & Kim, S., 2010. Regional moment tensor determination in the southern Korean Peninsula, *Geosci. J.*, **14**, 329–333.

Rivera, L. & Cisternas, A., 1990. Stress tensor and fault plane solutions for a population of earthquakes, *Bull. seism. Soc. Am.*, **80**, 600–614.

Rivera, L. & Kanamori, H., 2002. Spatial heterogeneity of tectonic stress and friction in the crust, *Geophys. Res. Lett.*, **29**, 12-1–12-14.

Scholz, C.H., 2002. *The Mechanics of Earthquakes and Faulting*, Cambridge Univ. Press.

Sibson, R.H., 1974. Frictional constraints on thrust, wrench and normal faults, *Nature*, **249**, 542–544.

Stein, R.S., 1999. The role of stress transfer in earthquake occurrence, *Nature*, **402**, 605–609.

Takahashi, M., Mizoguchi, K., Kitamura, K. & Masuda, K., 2007. Effects of clay content on the frictional strength and fluid transport property of faults, *J. geophys. Res.*, **112**.

Townend, J. & Zoback, M.D., 2006. Stress, strain, and mountain building in central Japan, *J. geophys. Res.*, **111**, doi:10.1029/2005JB003759.

Vavryčuk, V., 2014. Iterative joint inversion for stress and fault orientations from focal mechanisms, *Geophys. J. Int.*, **199**, 69–77.

Watts, A. & Ryan, W., 1976. Flexure of the lithosphere and continental margin basins, *Tectonophysics*, **36**, 25–44.

Yassir, N. & Rogers, A., 1993. Overpressures, fluid flow and stress regimes in the Jeanne d'Arc Basin, Canada, *Int. J. Rock Mech. Min. Sci. Geomech. Abstr.*, **30**, 1209–1213.

Yoon, S., Park, S. & Chough, S., 1997. Western boundary fault systems of Ulleung Back-arc Basin: further evidence of pull-apart opening, *Geosci. J.*, **1**, 75–88.

Zoback, M.D. & Townend, J., 2001. Implications of hydrostatic pore pressures and high crustal strength for the deformation of intraplate lithosphere, *Tectonophysics*, **336**, 19–30.

Zoback, M.L., 1992. Stress field constraints on intraplate seismicity in eastern North America, *J. geophys. Res.*, **97**, 11 761–11 782.